Journal of Materials Chemistry A

Aperture Control in Polymer-based Composites with Hybrid Core-Shell Spheres for Frequency-Selective Electromagnetic Interference Shielding

Journal:	*Journal of Materials Chemistry A*
Manuscript ID	TA-ART-01-2022-000045.R1
Article Type:	Paper
Date Submitted by the Author:	01-Mar-2022
Complete List of Authors:	Hwang, Uiseok; Sungkyunkwan University, Department of Polymer Science and Engineering Kim, Junyoung; Sungkyunkwan University, Department of Energy Science Sun, Hanna; Sungkyunkwan University, Department of Energy Science Park, In-Kyung; Sungkyunkwan University, Department of Polymer Science and Engineering Suhr, Jonghwan; Sungkyunkwan University, School of Mechanical Engineering Nam, Jae-Do; Sungkyunkwan University, Department of Polymer Science and Engineering

ARTICLE

Aperture Control in Polymer-based Composites with Hybrid Core-Shell Spheres for Frequency-Selective Electromagnetic Interference Shielding†

Received 00th January 20xx,
Accepted 00th January 20xx

DOI: 10.1039/x0xx00000x

Uiseok Hwang,[a] Junyoung Kim,[b] Hanna Sun,[b] In-Kyung Park,[a] Jonghwan Suhr,[c] and Jae-Do Nam*[ab]

Next-generation electromagnetic interference (EMI) shielding technology requires a frequency-selective capability, which can enable shielding and/or passing electromagnetic (EM) waves of a certain frequency range. Herein, we propose a novel composite system that provides frequency-selective EM wave absorption capability using bimodal-sized hybrid core-shell spheres, which are a combination of two different types of mono-sized core-shell spheres. Both sphere types had polymer cores covered with shells of either wave-diffuse reflecting nickel/gold or wave-absorbing graphene. Notably, the composite exhibited an excellent EMI shielding effectiveness of 96.5 dB at 1 mm due to the synergistic effect of recursive multiple internal diffusive reflections and absorption induced by the spheres. Furthermore, the absorption frequency range and selectivity of EM waves can be controlled in the 8.2–12.4 GHz frequency range by tuning the aperture size, which is specified by the ratio of two types of spheres in the composite. The developed hybrid core-shell spheres and their composites can be tailored with various types of matrices and have enormous potential for special applications, including advanced EMI shielding materials.

Introduction

As electronic devices and equipment with highly integrated circuits are being increasingly used in automotive, aerospace, and military applications, the harmful effects of electromagnetic (EM) radiation have become a primary concern in device design and utilization. Electromagnetic interference (EMI) from electronic components perturbs the signals leading to device malfunction, besides affecting human health.[1–3] EM pollution in various frequency bands has prompted fundamental research on smart frequency-selective EMI shielding materials, which could selectively absorb, reflect, and/or pass the EM waves in a specific frequency range.[4–6]

EMI shielding materials with tunable frequency selectivity can replace conventional materials in various fields, including self-driving cars, civil/military aircrafts, 5G communication, etc. Specifically, in an environment where various EM waves exist over a broad frequency spectrum, such materials can selectively shield the interfering EM waves in undesirable frequency ranges and transmit them in telecommunication frequency ranges, enabling vehicles to smoothly communicate without device malfunction. For instance, stealth systems in military applications require advanced radar-absorbing materials (RAMs), which is an important aspect of EMI shielding. A stealth aircraft should absorb EM waves in the X-band frequency range (8–12 GHz), so that the waves do not bounce back to the enemy radar detectors, as X-band is a relatively prominent frequency range in modern radars.[7] Accordingly, materials for selective absorption in the X-band can be applied to stealth aircraft, replacing a bandpass frequency-selective surface (FSS) that utilizes reflection for out-of-band waves.[8]

Unfortunately, such technology has rarely been reported because most EMI shielding materials exhibit low frequency selectivity. To impart this unique functionality, the structural ‘aperture’ size of materials, which is provided by the interstitial space of the shielding material, should be controlled, where the resonance of EM waves of a specific wavelength is triggered.[4] Recently, several pioneering works have suggested sandwich[4,5] and stretchable conductive segregated structures[6] with different thicknesses that serve as apertures. However, they required samples of varying thickness to shield the EM waves at different frequencies, and their shielding frequency and selectivity were difficult to control. Therefore, well-defined aperture size is essential to control the shielding frequency and determine whether the EM waves of specific wavelength will pass through the material or not.

Considering that polymer-matrix composites with embedded conductive nanofillers have been intensively explored in recent years owing to their lightweight, easy processability, and material design flexibility, novel frequency-selective materials can also be realized in the form of composites.[9–12] Their fillers should provide controllable aperture size as well as have isotropic shapes to block the EM waves in a specific frequency range in an isotropic manner for different incident angles. For

[a]*Department of Polymer Science and Engineering, Sungkyunkwan University, Suwon 16419, Republic of Korea. E-mail: jdnam@skku.edu*
[b]*Department of Energy Science, Sungkyunkwan University, Suwon 16419, Republic of Korea*
[c]*School of Mechanical Engineering, Sungkyunkwan University, Suwon 16419, Republic of Korea*
† Electronic supplementary information (ESI) available. See DOI: 10.1039/x0xx00000x

such purposes, a core-shell-structured polymer sphere is one of the best candidates in a novel composite system, where the mono-sized cores are covered with various EMI shielding materials, such as metal, metal oxide, MXene, carbon nanotube, and graphene.[13–21] The distances between the spheres in polymer matrices can be the key factor for controlling the shielding frequency range without the need for varying the thickness, as the aperture size of the composite structure can be precisely controlled by regulating the type and weight fraction of spheres. Thus, the passage of EM waves can be selectively blocked by the specific size of the aperture, which is dictated by the spatial configuration of mono-sized spheres in terms of packing density and particle size.

In view of the two main shielding mechanisms of reflection and absorption, shell materials for the spheres can be judiciously chosen. Metals are good EMI shielding materials that utilize reflection. These materials with high electrical conductivity reflect EM waves via direct interaction with free electrons, thereby dissipating the radiation power of those waves.[22–24] The metallic barrier reflects the incident EM waves to the surroundings instead of absorbing them.[25] On the other hand, nanomaterials such as MXene sheets and carbon-based materials can attenuate EM radiation via reflection and absorption as their electric and/or magnetic dipoles are capable of transforming EM energy to thermal energy.[26–29] The focus of EMI shielding composites research has largely been limited to the effects of filler type or concentrations, and little emphasis has been placed on controlling the shielding mechanism or frequency selectivity.

Among the candidate materials, nickel/gold multi-shelled polymer spheres, which are widely used in the application of anisotropic conductive films, can be employed to control the aperture in polymeric composites with their well-known high mechanical properties and electrical conductivity originating from the nickel and gold shells, respectively.[13] Also, the graphene or MXene sheets have been easily coated on polymer spheres via electrostatic self-assembly to form segregated composites with the deformability of the polymer cores above the glass transition temperatures.[9,14] If both EM wave-absorbing and reflecting spheres are used in polymer matrices, the contribution of absorption and reflection may be controlled by tuning the ratio of the two fillers. Moreover, the unique combination could provide a dramatically enhanced shielding effectiveness (SE) with higher absorption via infinite internal multiple reflections and absorption,[30] ultimately eliminating the EM waves in a specific frequency range.

In this study, we investigated a novel composite system containing two different types of core-shell spheres. Graphene- and nickel/gold-shelled polymer spheres with sizes of 200 nm and 20 μm were chosen as the wave-absorbing and wave-reflecting fillers as they were considered to provide wave-absorbing nano-networks and well-defined apertures in a precise manner, respectively. Each sphere was prepared via electrostatic self-assembly and electroless deposition, respectively. Hybrid core-shell sphere-filled composites were fabricated by simply mixing the spheres with epoxy resin, followed by compression molding. The EMI shielding performance and frequency selectivity of the composites were thoroughly investigated. The absorption range and selectivity could be controlled in the X-band frequency range by regulating the ratio of the two types of spheres in the composites.

Results and discussion

Fig. 1a illustrates the overall strategy for hybrid core-shell sphere composites, including the fabrication sequences of the two different types of core-shell spheres. First, graphene-wrapped polystyrene (PS) spheres (Graphene@PS) were prepared via the electrostatic self-assembly of positively charged *p*-phenylenediamine (PPD)-reduced graphene oxide sheets on anionic polystyrene spheres. On the other hand, nickel and gold shells were sequentially deposited on poly(methyl methacrylate) (PMMA) spheres (Ni/Au@PMMA) via electroless plating in the presence of palladium nanoparticles as a catalyst. Finally, the core-shell spheres were mixed with epoxy resin and compression-molded to yield the composites.

Metallic shells scatter the incident EM waves with their curved surfaces, whereas graphene shells can absorb some waves. Therefore, the mixture of these two core-shell spheres is quite advantageous for EMI shielding, given their specific shielding effects and isotropic characteristics. When incident EM waves arrive at the surface of a Ni/Au@PMMA sphere, they are immediately reflected because of the large number of free electrons on the highly electrically conductive surface of the metal shells. The reflected EM waves are partially absorbed by the neighboring Graphene@PS spheres, resulting in attenuation. The residual EM waves undergo multiple diffuse reflections in random directions among the adjacent Ni/Au@PMMA spheres before final absorption into the Graphene@PS spheres. Thus, through this recursive process, the EM waves can be substantially eliminated and thermally dissipated.

The PS cores were negatively charged over the entire pH range, as shown by the zeta potential curve (Fig. 1b), which was attributed to the carboxyl groups from the methacrylic acid (MAA) comonomer and sulfate groups from the potassium persulfate (KPS) initiator on the surface. On the other hand, graphene was positively charged in the pH range of 2–6, owing to the presence of amine groups from the reducing agent (PPD)[31] (Fig. 1a). At a pH of 4, the PS spheres and graphene sheets had high dispersion stability (inset of Fig. 1b) due to their strong repulsive forces as suggested by zeta potential values of −43.9 mV and 31.7 mV, respectively. When the graphene dispersion was slowly added to the diluted PS emulsion under vigorous stirring, the PS spheres were rapidly covered by the graphene sheets via electrostatic attraction until the neutralizing net surface charge reached approximately −10 mV.[17,18] The destabilized core-shell spheres were subsequently flocculated by gravity, leaving a transparent solution at the top of the bottle. At this destabilization point, the weight fraction of graphene in the Graphene@PS spheres was 2.05 wt.%.

Considering that wave-reflecting spheres determine the aperture size of polymer composites, while wave-absorbing spheres constitute the EM wave-sink network, mono-sized polymer particles with average diameters of 20 μm and 200 nm were used as their respective cores (Fig. S1†). The morphology

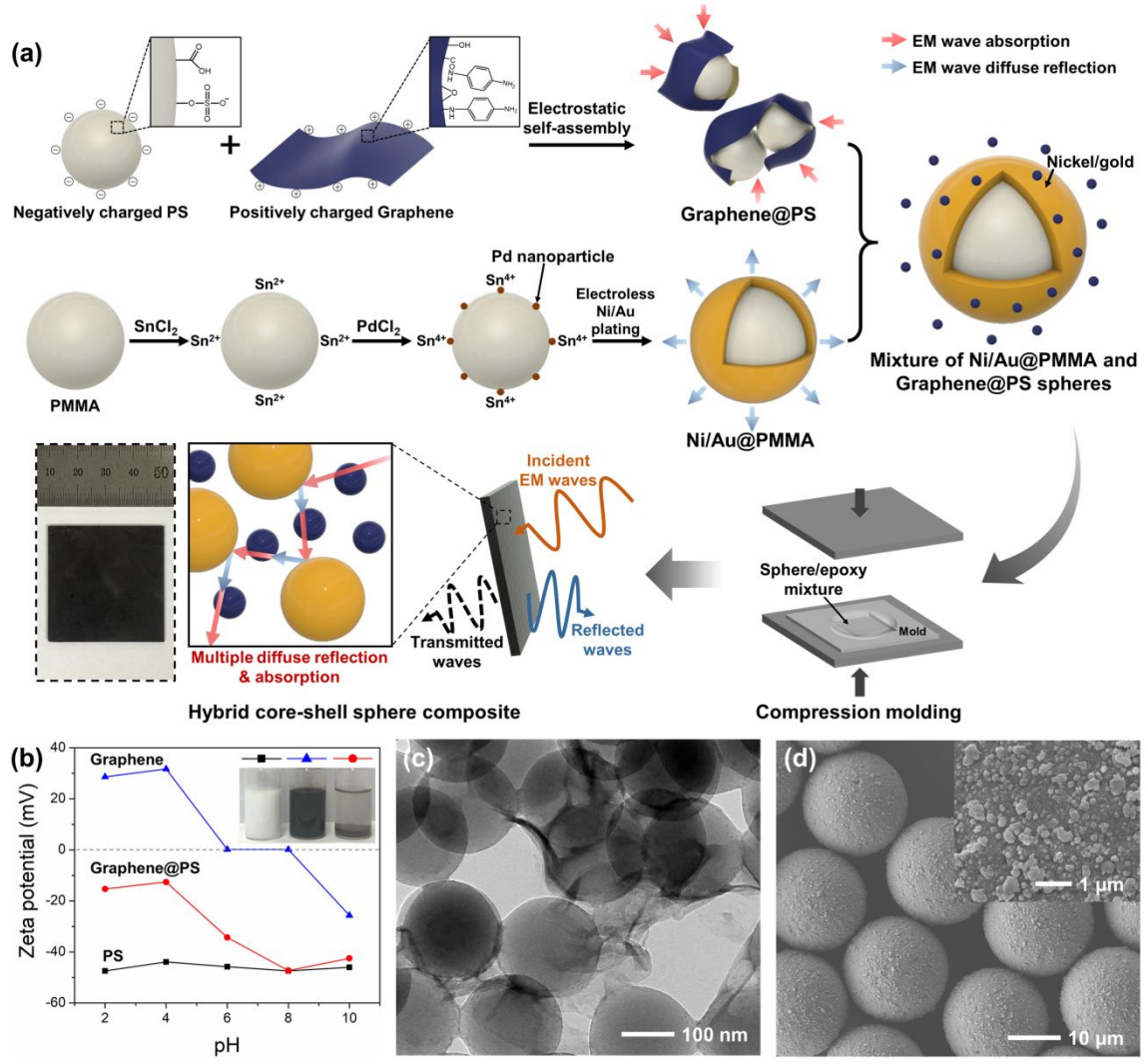

Fig. 1 (a) Schematic illustration of the fabrication process and proposed EMI shielding mechanism of hybrid core-shell sphere composites; Inset: Digital image of an as-synthesized core-shell sphere composite. (b) Zeta potential of PS, graphene, and Graphene@PS; Inset: Digital image of the corresponding 2 wt.% aqueous dispersions at pH 4. (c) HRTEM image of Graphene@PS spheres. (d) FE-SEM images of Ni/Au@PMMA spheres at different magnifications.

and structure of Graphene@PS spheres were investigated by high-resolution transmission electron microscopy (HRTEM) and field-emission scanning electron microscopy (FE-SEM) (Fig. 1c and Fig. S2†). The surface of the graphene-wrapped PS spheres was wrinkled and rough owing to the presence of thin graphene sheets. Some of the spheres were inter-linked by the graphene sheets, forming large three-dimensional clusters, with graphene sheets larger than the PS core particles. These core-shell structures can facilitate the homogeneous dispersion of graphene in polymer matrices, effectively preventing agglomeration of the graphene sheets.[32]

Fig. S3† and Fig. 1d show the surfaces of Ni@PMMA and Ni/Au@PMMA spheres, respectively. Both the particles were uniform in size and had rough surfaces compared to their PMMA cores, indicating the formation of metal shells. Each continuous coating layer was composed of sub-500 nm granules, as shown in the inset images in Fig. S3† and Fig. 1d, respectively. However, they exhibited different surface morphologies with the surface of the Ni/Au shell rougher than that of the Ni shell. Moreover, energy-dispersive X-ray spectroscopy (EDS) elemental mappings of the Ni@PMMA and Ni/Au@PMMA spheres confirmed that the nickel and gold shells were successfully constructed on cores, respectively (Fig. S4 and S5†).

The Ni/Au@PMMA and Graphene@PS core-shell spheres were mixed in different weight fractions and ratios to yield bimodal-sized hybrid core-shell spheres. The FE-SEM images at different magnifications show the morphology of the mixture and clearly demonstrate the size difference between the spheres (Fig. S6†). The interstitial spaces between the Ni/Au@PMMA spheres were filled with numerous Graphene@PS spheres, which were one hundred times smaller than the Ni/Au@PMMA spheres. The wrinkled graphene sheets were dispersed among the PS spheres, with their surfaces in contact with the particles (Fig. S6b†).

The formation and compositional characterizations of the as-prepared Graphene@PS and Ni/Au@PMMA core-shell spheres were evaluated using X-ray photoelectron spectroscopy (XPS), Raman spectroscopy, and X-ray diffraction (XRD), as shown in Fig. 2. Both graphene and Graphene@PS exhibited N1s peaks at 400 eV, which mainly arose from the amine groups of the PPD molecules grafted onto the graphene surface. The Graphene@PS

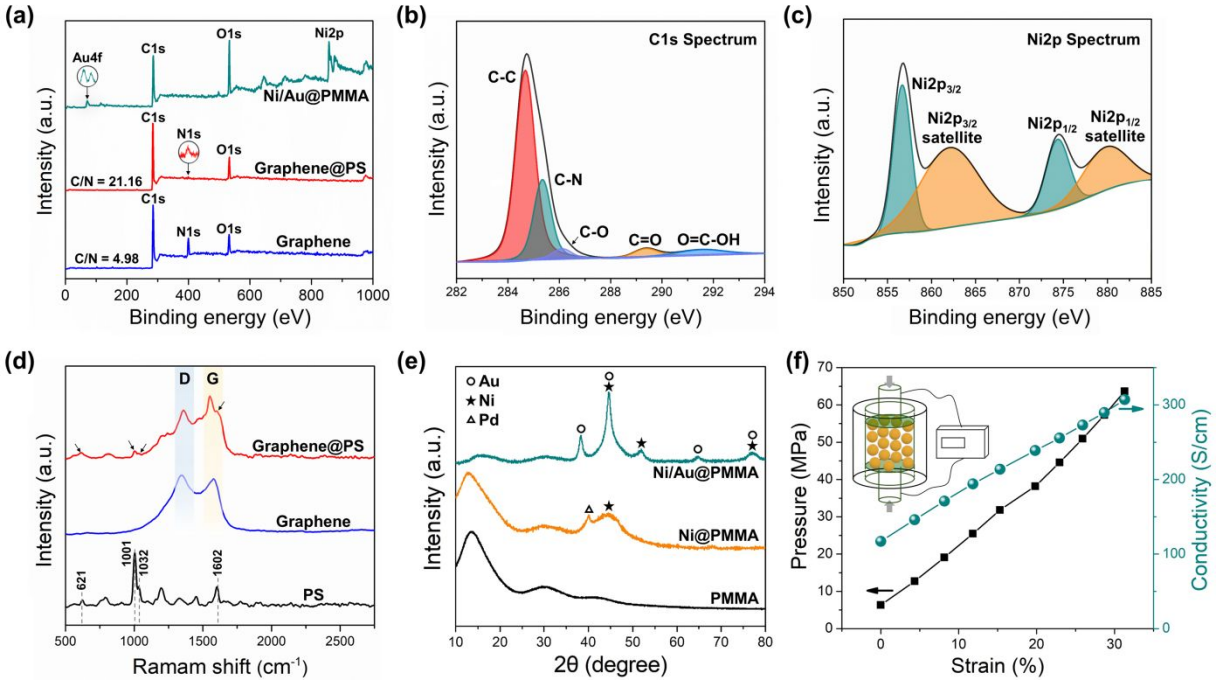

Fig. 2 (a) XPS spectra of graphene, Graphene@PS, and Ni/Au@PMMA. (b) XPS C1s core-level spectra of Graphene@PS spheres. (c) XPS Ni2p core-level spectra of Ni/Au@PMMA spheres. (d) Raman spectra of PS, Graphene, and Graphene@PS. (e) XRD patterns of PMMA, Ni@PMMA, and Ni/Au@PMMA spheres. (f) Pressure and electrical conductivity for Ni/Au@PMMA spheres plotted as a function of compressive strain with inset showing schematic of the powder resistivity measurement system.

spheres had a higher C/N ratio (21.16) than graphene sheets (4.98), due to carbon-based nature of PS particles. The deconvoluted C1s spectrum of Graphene@PS showed peaks at 284.7, 285.3, 286.1, 289.4, and 291.5 eV, corresponding to C–C, C–N, C–O, C=O, and O=C–OH bands, respectively (Fig. 2b). An intense C–N peak was also found in the C1s spectrum of graphene, indicating that the N element originated from the graphene sheets (Fig. S7†).[31] Meanwhile, Ni and Au elements were found in the Ni/Au@PMMA spheres, stemming from nickel and gold sequential shells, respectively (Fig. 2a). The bimodal peaks at 83.5 and 87.2 eV were assigned to the $Au4f_{7/2}$ and $Au4f_{5/2}$, respectively. The fitting curves of the Ni2p spectrum showed two main peaks at 856.7 and 874.4 eV and corresponding satellite peaks at 862.2 and 880.2 eV, which were assigned to $Ni2p_{3/2}$ and $Ni2p_{1/2}$, respectively (Fig. 2c).

Fig. 2d presents the Raman spectra of PS, graphene, and Graphene@PS from 500 to 3000 cm^{-1}. Strong D (1340 cm^{-1}) and G (1581 cm^{-1}) bands were observed for the graphene sheets. The intensity ratio of the two bands (I_D/I_G) was 1.11, which can be used to evaluate the degree of reduction of graphene oxide.[33] The typical Raman spectrum of PS exhibited C–C–C ring deformation (621 cm^{-1}), C–C ring breathing (1001 cm^{-1}), in-plane C–H deformation (1032 cm^{-1}), and ring stretching (1602 cm^{-1}). In the spectrum of the Graphene@PS spheres, peaks from both graphene and PS were observed.

The XRD patterns of PMMA, Ni@PMMA, and Ni/Au@PMMA spheres are shown in Fig. 2e. Three broad diffraction peaks at 13.6°, 30.1°, and 42.5° were observed for the PMMA spheres, with typical characteristics for amorphous materials. The XRD pattern of Ni@PMMA exhibited two additional peaks at 40.1° and 44.6°, corresponding to the diffractions of (111) planes of Pd and Ni, respectively. Remarkably, after the gold layer deposition on the surface of the Ni@PMMA spheres, the XRD pattern for the Ni/Au@PMMA spheres showed typical peaks indexed to those of Ni (JCPDS No. 04-0850) and Au (JCPDS No. 04-0784), suggesting the sequential formation of nickel and gold shells. Moreover, the absence of diffraction peak of Pd indicated that the surface of the PMMA spheres was fully covered by the metal shells. The weight fractions of nickel and gold in Ni/Au@PMMA spheres were 19.03 wt.% and 1.36 wt.%, respectively, as confirmed by inductively coupled plasma-optical emission spectroscopy (ICP-OES).

Fig. 2f and the inset show the pressure and electrical conductivity of Ni/Au@PMMA spheres plotted as a function of strain and the schematic of the powder resistivity measurement system, respectively. Both the pressure and electrical conductivity increased linearly with strain. The spheres exhibited a pressure and conductivity of 63.7 MPa and 30,705 S/m, respectively, at 31.3% strain. The increasing electrical conductivity of Ni/Au@PMMA spheres with strain could stem from the high packing density of the spheres and the increase in the contact area between the spheres. Additionally, the absence of noisy signals in the curves implied that delamination at the metal-polymer interfaces of the surfaces did not occur under the given strain.

The hybrid core-shell sphere composites were fabricated by mixing the spheres with epoxy resin, followed by compression molding. The composites were labeled as M00, G00, and M00/G00 (00 = from 10 to 70, corresponding to the weight fractions of the Ni/Au@PMMA and Graphene@PS spheres in the composites). The weight compositions of the composites are listed in Table S1†. Fig. S8† shows the fractured surface of the M60/G10 composite, providing insight into its structural formation. The embedded Ni/Au@PMMA core-shell spheres with rough surfaces were observed without particle aggregation

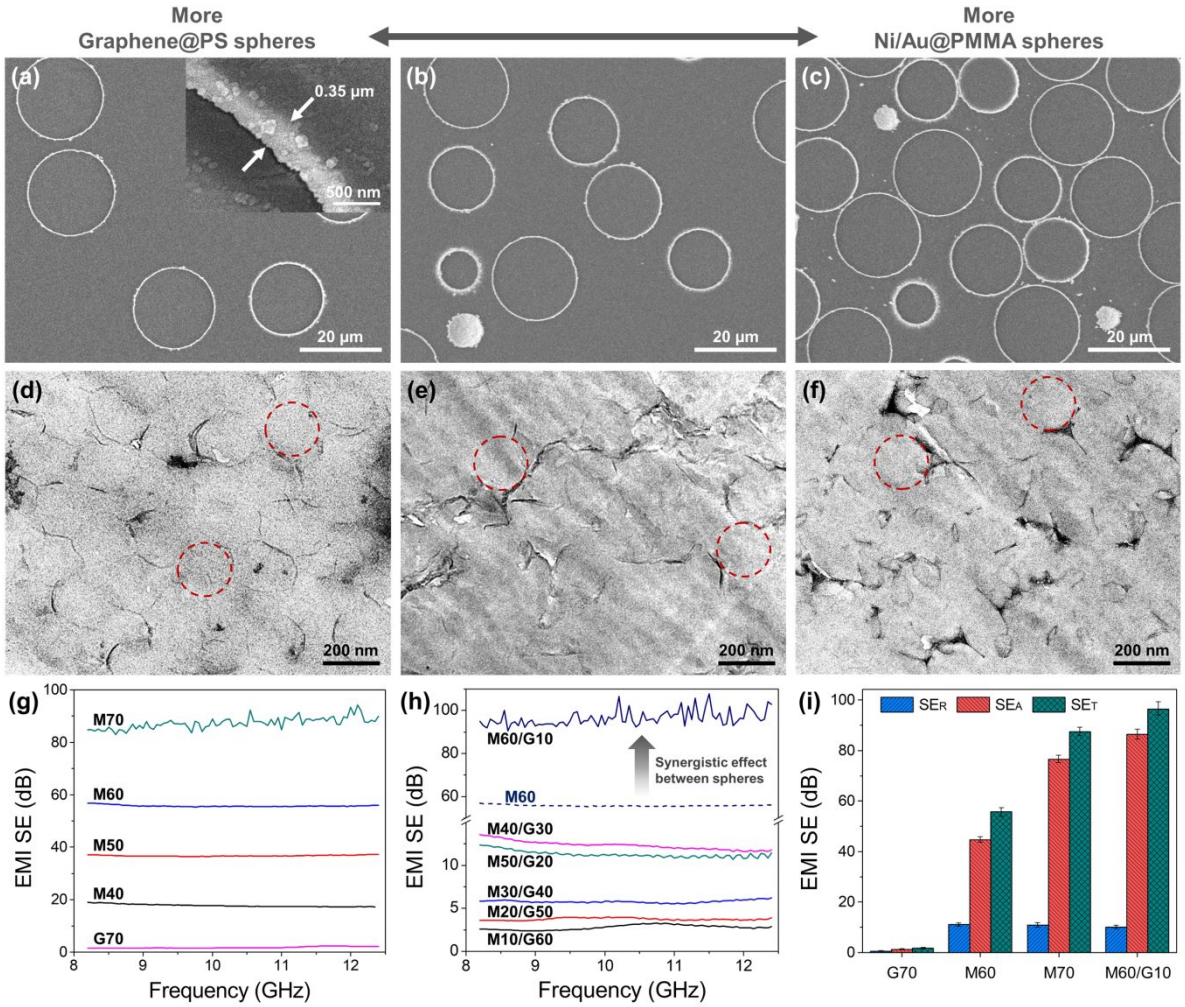

Fig. 3 FE-SEM images of polished cross-sections of (a) M10/G60, (b) M30/G40, and (c) M60/G10 composites. HRTEM images of ultrathin sections of (d) M10/G60, (e) M30/G40, and (f) M60/G10 composites. EMI SE_T of 1-mm-thick (g) M00 and (h) M00/G00 composites. (i) Comparison of average SE_T, SE_A, and SE_R of different core-shell sphere composites in the X-band frequency range.

or shape deformation, which could provide well-defined aperture sizes in terms of packing density of the spheres. The spheres retained their original shape despite the high-pressure and -temperature conditions due to the high glass transition temperature (T_g = 125°C) of their cross-linked PMMA cores, as confirmed by differential scanning calorimetry (DSC) analysis (Fig. S9†).

The polished cross-sections of the core-shell sphere composites with various weight compositions are compared in Fig. 3a–c. The presence of Ni/Au@PMMA spheres was confirmed by the presence of circular metal shells with an average thickness of 0.35 μm (inset of Fig. 3a). The metal rings had various sizes of up to 20 μm, depending on the point at which the Ni/Au@PMMA spheres were cut. With the increasing weight fraction of the Ni/Au@PMMA spheres in the composites, the number of rings (metal shells of Ni/Au@PMMA sphere) also increased. Particularly, in the case of the M60/G10 composite, some contact points between the rings were observed, which would provide electrically conductive paths across the metal shells (Fig. 3c). The empty regions between the Ni/Au@PMMA spheres in each sample were filled with Graphene@PS spheres and epoxy resin.

To analyze the dispersion state of Graphene@PS spheres in the epoxy matrix, ultrathin sections of the composites were characterized using HRTEM (Fig. 3d–f). The spaces between the PS blocks (red lines) contained the graphene sheets due to separation effects, enabling homogeneous dispersion of the ultrathin graphene without any agglomeration.[9,32] Owing to the presence of epoxy resin between the Graphene@PS spheres, the graphene network was partially connected. In the M10/G60 composite, the Graphene@PS spheres were compressed into clusters, exhibiting a deformed hexagonal block structure (Fig. 3d and Fig. S10†). With decreasing Graphene@PS sphere content, the graphene networks were less connected. In the case of M60/G10 composite, graphene circles of various sizes (<200 nm) were observed (Fig. 3f). The overall structure of the hybrid core-shell sphere composite was further confirmed using HRTEM, clearly showing both the Ni/Au shell and the Graphene@PS spheres (Fig. S11†). In the presence of the metallic shells and three-dimensional graphene networks, the incident EM waves are considered to be attenuated by synergistic effects between them, as schematically shown in Fig. 1a.

The total EMI SE (SE_T) of G70 and M00 composites was first measured in the X-band frequency range to evaluate the EMI shielding ability of Graphene@PS and Ni/Au@PMMA

core-shell spheres, respectively (Fig. 3g). The SE_T of G70 composite was relatively low (<3 dB), transmitting over 50% of the incident EM waves, whereas that of M00 composites significantly improved with increasing Ni/Au@PMMA sphere content. An average SE_T of 17.8 dB, which satisfies some commercial EMI shielding requirements, was obtained with the M40 composite. This value linearly increased to 55.7 dB for the M60 composite. The M70 composite exhibited an extremely high SE_T of 87.4 dB with an electrical conductivity of 14,768 S/m, which could block approximately 99.9999998% of incident EM radiation with only 0.0000002% transmission. The extraordinary EMI shielding performance was attributed to the presence of highly electrically conductive networks formed by connected metal shells within the composites.

Subsequently, the synergistic effect of the Ni/Au@PMMA and Graphene@PS spheres in the M00/G00 composites was investigated (Fig. 3h). The total amount of core-shell spheres in each composite was fixed at 70 wt.%. Both the electrical conductivity and SE_T may be closely related to the ratio of the two types of core-shell spheres. It was found that the addition of Graphene@PS spheres to M00 composites decreased the electrical conductivity of the composite, which could eventually provide a lower SE_T. For instance, the electrical conductivity of the M60/G10 composite (4,831 S/m) was much lower than that of the M60 composite (12,183 S/m). The average SE_T of the M00/G00 composites gradually increased from 2.8 to 12.3 dB as the weight fraction of Ni/Au@PMMA spheres increased from 10 to 50%. In the case of M50/G20 and M40/G30 composites, the addition of Graphene@PS spheres decreased the performance in comparison to the corresponding M50 and M40 composites, which contained the same amount of Ni/Au@PMMA spheres. Remarkably, the SE_T of the M60/G10 composite was 96.5 dB, which is interesting as this composite exhibited even higher SE_T than the M60 composite (55.7 dB) despite much lower electrical conductivity. Therefore, it was indicated that the synergistic effect on EMI shielding reaches a maximum for the sphere ratio in the M60/G10 composite, and it was inferred that the M60/G10 composite had an optimal structural arrangement, which could trap the incident EM waves and subsequently eliminate them by infinite internal multiple diffuse reflections and absorption.

The SE_T and SE values caused by absorption (SE_A) and reflection (SE_R) for various samples are shown in Fig. 3i, clearly comparing the EMI shielding mechanism of the composites. It was anticipated that a higher content of electrically conductive Ni/Au@PMMA spheres would enhance the contribution of reflection (SE_R) for the M70 composite compared to the M60 composite. However, it caused only an increment in SE_A, while maintaining the SE_R. Note that the synergistic effect of the Ni/Au@PMMA and Graphene@PS core-shell spheres is the key factor that ensures a superior EMI SE of the M60/G10 composite. The addition of Graphene@PS spheres in the composite reduced the SE_R from 11.1 to 10.1 dB and increased the SE_A from 44.6 to 86.4, subsequently increasing the SE_T from 55.7 to 96.5 dB compared to the M60 composite. The reflection, absorption, and transmission fractions of the composites are summarized in Table S2†.

To realize frequency-selective EMI shielding, i.e., controlling the contribution of transmission, reflection, and absorption in different frequency ranges, M00/G00 composite was combined with G70 composite, yielding 2-mm-thick bilayer-structured composites (M00/G00+G70), where the M00/G00 layer presented a controlled aperture size with different weight fractions of Ni/Au@PMMA spheres and the Graphene@PS sphere-based G70 layer acted as a dielectric spacer to trigger the absorption of specific EM waves with structural resonance features.[4,5,34] The SE_T of the bilayer composites had a similar tendency as that of M00/G00 composites except for the decreased SE_T of the M60/G10+G70 bilayer composite from 96.5 to 68.0 dB (Fig. 4a). Interestingly, there was a notable change in frequency dependency for the bilayer composites across the measured frequency range, which was not observed in the G70, M00, and M00/G00 composites and most conventional EMI shielding materials. The wave-shaped curves shifted to a lower frequency range as the weight fraction of Ni/Au@PMMA sphere increased.

The shielding mechanisms (transmission, absorption, and reflection) of the different composites are shown in Fig. 4b and Table S3†. At a lower content of Ni/Au@PMMA spheres in the M00/G00 layer, the transmission fraction of the bilayer composite increased, indicating that some incident EM waves leaked due to the large aperture size, specified by the distances between the mono-sized metallic spheres (schematic in the inset of Fig. 4b). In the case of the M60/G10+G70 bilayer composite, almost all EM waves were blocked by the packed metallic spheres without leakage of the waves. Notably, the absorption fraction curves of the bilayer composites gave peaks (labeled as f_s) with the highest absorption values. This means that the bilayer composites could be used as frequency-selective EMI shielding materials that utilize absorption. The f_s values for the M30/G40+G70, M40/G30+G70, and M60/G10+G70 bilayer composites were 9.9, 9.6, and 11.3 GHz, respectively, with corresponding absorption fractions of 59.7, 69.1, and 76.1%, respectively.

The M00/G00 composites absorbed <35% of the incident EM waves with little frequency selectivity (Fig. S12†). By contrast, with the addition of the G70 layer, the absorption capability and selectivity of the bilayer composites increased substantially, as shown in Fig. 4c. To specify the frequency-selective absorption properties of the bilayer composites, the absorption selectivity and absorption selectivity parameter can be defined as follows:

$$\text{Absorption selectivity} = \frac{A}{A_{min}} \quad (1)$$

$$\text{Absorption selectivity parameter, } \alpha = \frac{A_{max}}{A_{min}} \quad (2)$$

where A is the absorption fraction, and A_{min} and A_{max} are the minimum and maximum values of the absorption fraction, respectively, in the measured frequency range. These factors could be easily obtained by dividing the A and A_{max} values by the A_{min} values, as shown in Fig. 4d and 4e, respectively.

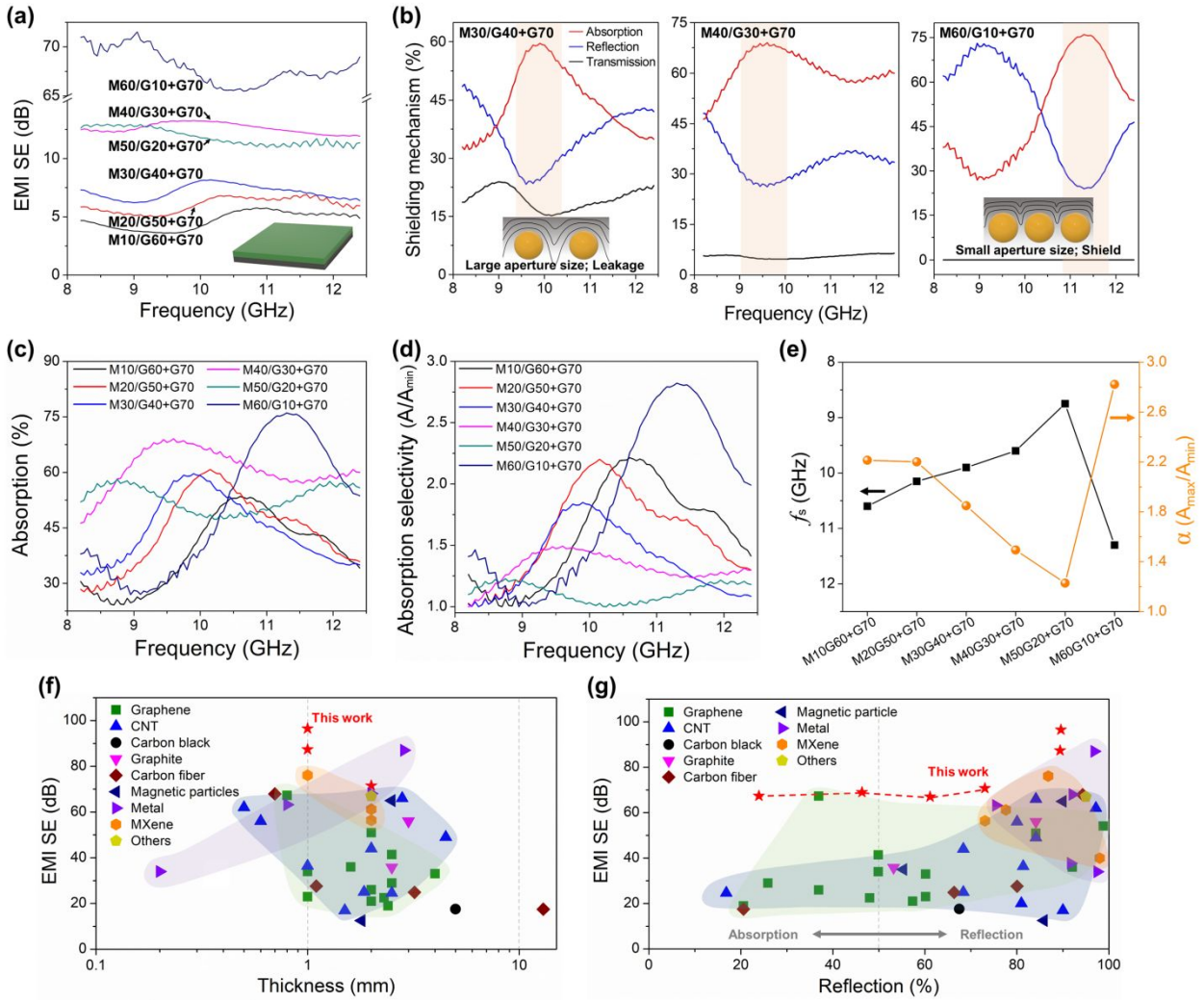

Fig. 4 (a) EMI SE_T of 2-mm-thick M00/G00+G70 bilayer composites. (b) Shielding mechanism of different bilayer composites with suggested effects of aperture size. (c) Absorption fraction and (d) absorption selectivity (A/A_{min}) of the bilayer composites as a function of frequency. (e) f_s and absorption selectivity parameter (α) as a function of weight composition of M00/G00 layer of the bilayer composites. SE_T comparison between hybrid core-shell sphere composites and previously reported polymer composites according to (f) sample thickness and (g) shielding mechanism.

Surprisingly, f_s and absorption selectivity of the bilayer composites were dependent on the weight composition of the M00/G00 layer. The M60/G10+G70 bilayer composite had the highest absorption selectivity of over 2.5 in the frequency range of 10.8–11.8 GHz, whereas the M50/G10+G70 bilayer composite was relatively frequency-independent (Fig. 4d). The α decreased with increasing weight fraction of Ni/Au@PMMA spheres from 10 to 50%, corresponding to a decrease in that of the Graphene@PS spheres from 60 to 20% (Fig. 4e). The M60/G10+G70 bilayer composite had a maximum α value of 2.82, indicating that it absorbed 2.82 times more EM waves at 11.3 GHz than at the point of least absorption in the X-band range. These results confirmed that the absorption frequency range and EMI shielding selectivity could be precisely controlled by tuning the ratio of Ni/Au@PMMA and Graphene@PS spheres in the composite.

The novelty of hybrid core-shell sphere composites was further highlighted through a comprehensive comparison with previously reported polymer composites (Fig. 4f and 4g; Table S4†). Although metal and thin films of pure MXene and graphene typically show high EMI shielding performance,[35,36] their composites exhibit reduced SE_T due to the presence of insulating polymer matrices.[24,37] By contrast, the 1-mm-thick M70 and M60/G10 composites exhibited extremely high SE_T with metal and/or graphene contents of 14.27 and 12.44 wt.%, respectively, which is one of the best EMI shielding performances among all the polymer composites of comparable thicknesses (Fig. 4f). In MXene and graphene composites, reflective interfaces are constructed by two-dimensional MXene and graphene nanosheets, respectively, which cause multiple internal reflection effects in the through-plane direction.[35] By contrast, the core-shell sphere composites have reflective interfaces of numerous metallic shells, enabling recursive internal diffusive reflections in random directions. Notably, multiple reflections in random directions can be more efficient than in the through-plane direction for EMI shielding performance because incident EM waves have to travel a longer path in the material, which is more likely to cause attenuation.

Additionally, the EMI shielding mechanisms of all the composites were compared. Generally, SE_A and SE_R, which are

calculated using the absorption and reflection coefficients, respectively, are used as standards to evaluate the EMI shielding mechanism (Note S1†). However, the SE_A and SE_R values are insufficient and sometimes confusing to evaluate the mechanism because the absolute contribution of absorption and reflection cannot be obtained from a simple comparison. In fact, an EM wave-reflecting material can exhibit a larger SE_A than SE_R (Note S2†).[38] Therefore, the reflection and absorption fractions for incident EM waves are more relevant parameters for evaluating the shielding mechanism of materials. As shown in Fig. 4g, the EMI shielding composites were compared for their reflection fractions, which are the proportions of reflection for incident EM waves. The portion that is not reflected is almost entirely absorbed because EMI shielding materials have transmission fractions of nearly zero.[39] Thus, a reflection fraction of 50% can be used as a criterion to classify materials with a dominant shielding mechanism. Among the known materials with a SE_T of over 60 dB, hardly any are absorption-dominant shielding materials. Specifically, typical polymer composites of MXene (orange) and metal (violet) exhibit high SE_T with reflection-dominant shielding mechanisms, whereas those of graphene (green) show relatively low SE_T with absorption-dominated feature. Notably, the M60/G10+G70 bilayer composite showed wide-ranging shielding mechanisms (from absorption to reflection) with higher SE_T values in different frequency ranges. This means that the bilayer composites can be used as both EM wave-absorbing and -reflecting materials, depending on the applied frequency range.

Conclusions

A unique composite structure was developed using a hybrid mixture of Ni/Au@PMMA and Graphene@PS core-shell spheres, which provided outstanding EMI shielding performance with tunable frequency selectivity. The synergistic effect of the two types of spheres is advantageous in EMI shielding with their recursive internal diffusive reflection and absorption mechanisms, as confirmed by the excellent EMI SE of their composites. In a bilayer configuration, the core-shell sphere composites displayed frequency-selective EM wave absorption capability with controlled aperture sizes. The absorption frequency range and selectivity could be precisely controlled in the X-band region by regulating the ratio of the two types of spheres. These results demonstrate a promising technique for fabricating advanced EMI shielding materials for various sophisticated applications and present a new paradigm in frequency-selective EMI shielding materials.

Experimental section

Materials

PPD-reduced graphene oxide was synthesized according to a previously reported method.[31] A dispersion of PPD-reduced graphene oxide in ethanol (UCMG-P10, 1.09 wt.%) was purchased from Best-Graphene Co. Ltd. (Korea). The crosslinked PMMA microspheres (average diameter = 20 μm) were supplied by Duksan Hi Metal Co. Ltd. (Korea). Styrene (purified prior to use), KPS, palladium (II) chloride, ammonium hydroxide solution (28 wt.%), and diethylenetriamine (DETA) were purchased from Sigma-Aldrich (USA). MAA, tin (II) chloride dihydrate, sodium borohydride ($NaBH_4$), and ammonium chloride were purchased from Junsei Chemical (Japan). Sodium hypophosphite monohydrate, nickel (II) sulfate hexahydrate, and sodium citrate were purchased from Daejung Chemical (Korea). Bisphenol A diglycidyl ether (DGEBA, YD-128) was purchased from Kukdo Chemical Co. Ltd. (Korea).

Synthesis of anionic PS microspheres

To obtain negatively charged polymer cores, soap-free emulsion copolymerization of styrene and MAA was conducted using the anionic initiator (KPS). Deionized water (5.5 L), styrene (1 L), and MAA (75 mL) were mixed in a 10 L four-necked reaction vessel equipped with a mechanical stirrer, thermometer, reflux condenser, and N_2 inlet. The mixture was purged with nitrogen gas, stirred at 200 rpm, and heated to 75℃. KPS solution (15 g of KPS dissolved in 500 mL of deionized water) was added to initiate polymerization. The reaction was performed at 75℃ and after 6 h, the mixture was cooled to room temperature.

Preparation of Graphene@PS core-shell spheres

Graphene@PS spheres were prepared via electrostatic self-assembly of positively charged reduced graphene oxide and anionic PS microspheres. The graphene dispersion (16 mL) was diluted with deionized water (400 mL) and tip-sonicated for 6 h, resulting in a stable dispersion. The diluted graphene dispersion was added dropwise into the PS emulsion (80 mL) diluted with 800 mL of deionized water under vigorous stirring at pH 4. After stirring, the Graphene@PS spheres were flocculated by destabilizing the dispersion, leaving a transparent solution at the top of the beaker. The resulting particles were filtered, washed with water several times, and collected via freeze-drying.

Preparation of Ni/Au@PMMA core-shell spheres

Shells of nickel and gold were sequentially constructed on PMMA spheres via an electroless deposition method, as reported previously.[13] First, the surface of PMMA microspheres (3 g) was sensitized using tin chloride dihydrate solution (0.1 M). The mixture was stirred for 30 min at room temperature. Afterward, the particles were separated from the solution and dispersed in a palladium chloride solution (50 mM) under stirring for 30 min at room temperature to give a palladium-ion-adsorbed surface for PMMA spheres. The palladium ions were reduced using a $NaBH_4$ solution (0.1 M) and the surface-treated spheres were repeatedly rinsed with water. Then, a nickel-plating solution was prepared by combining sodium hypophosphite (8 g), nickel sulfate hexahydrate (20 g), sodium citrate (50 g), ammonium chloride (25 g), and water (400 mL). The pH was adjusted to 8 using an ammonium hydroxide solution and the spheres were immersed in the plating solution at 60 ℃ for 2 h. Subsequently, electroless gold plating was performed in a gold plating solution (ICP Nicoro OCP, Okuno Chemical Co. Ltd., Japan) at 80 ℃ for 10 min. The microspheres in the fabrication process exhibited

different colors due to their different surface characteristics (Fig. S13†).

Fabrication of core-shell sphere composites

The core-shell spheres, Ni/Au@PMMA and Graphene@PS, were mixed with DGEBA and DETA (DGEBA/DETA = 10:1 w/w) in various weight ratios using a paste mixer three times for 1 min each. The mixtures were compression-molded in a hydraulic hot press at 35 MPa and 60℃ for 20 min. Then, the temperature was raised to 100℃ to cure the samples yielding various types of core-shell sphere composites.

Characterization

The size and structure of the samples were examined using FE-SEM (JSM 7401F, JEOL, Japan) and HRTEM (JEM-2100F, JEOL, Japan). The zeta potentials of the samples were measured via laser Doppler electrophoresis (Zetasizer Nano-ZS, Malvern, UK). The electrical resistivity of the Ni/Au@PMMA spheres was measured by the four-point probe method using a powder resistivity measurement system (MCP-PD51, Mitsubishi Chemical Analytech, Japan). The electrical resistivities of the core-shell sphere composites were measured with a four-point probe instrument (CMT-SR2000N, AIT Co. Ltd., Korea). The EMI SEs of the samples (40 mm × 40 mm × 1 mm) were measured in the frequency range of 8.2–12.4 GHz using a vector network analyzer (E5071C, Keysight Technologies, UK). The scattering parameters (S_{33}, S_{34}, S_{43}, and S_{44}) of each sample were recorded and used to calculate the EMI SE. XPS (ESCALAB 250, Thermo, USA) and Raman spectroscopy (alpha 300 M, 532 nm, WITec, Germany) were used to analyze the chemical elements and surface characteristics of the samples. The crystal structures of the samples were examined using XRD (D8 ADVANCE, Bruker, Germany) in the 2θ range of 10° to 80° with a scanning speed of 3° min^{-1}. The thermal transitions of the PMMA core of the Ni/Au@PMMA spheres were analyzed using DSC (DSC7020, Seiko Inst., Japan). ICP-OES (Varian, Austria) was used to quantify nickel and gold.

Conflicts of interest

There are no conflicts to declare.

Acknowledgements

This work was supported by a project from the U.S. Air Force Office of Scientific Research/AOARD (grant number: FA2386-19-1-4056), which was efficiently facilitated and technically advised by Dr. Tony Kim, the project's PO. We also appreciate the instrumental and financial support by a grant from the National Research Foundation of Korea (NRF-2019R1A2C1005922) and the Technology Innovation Program (KEIT-10080545 and KEIT-20013794 from MSIT and MOTIE, respectively).

References

1 J.-M. Thomassin, C. Jérôme, T. Pardoen, C. Bailly, I. Huynen and C. Detrembleur, *Mater. Sci. Eng.: R: Rep.*, 2013, **74**, 211–232.
2 A. Namai, S. Sakurai, M. Nakajima, T. Suemoto, K. Matsumoto, M. Goto, S. Sasaki and S.-i. Ohkoshi, *J. Am. Chem. Soc.*, 2009, **131**, 1170–1173.
3 B. Shen, W. Zhai and W. Zheng, *Adv. Funct. Mater.*, 2014, **24**, 4542–4548.
4 G. Wang, X. Liao, J. Yang, W. Tang, Y. Zhang, Q. Jiang and G. Li, *Compos. Sci. Technol.*, 2019, **184**, 107847.
5 W.-L. Song, C. Gong, H. Li, X.-D. Cheng, M. Chen, X. Yuan, H. Chen, Y. Yang and D. Fang, *ACS Appl. Mater. Interfaces*, 2017, **9**, 36119–36129.
6 W.-C. Yu, G.-Q. Zhang, Y.-H. Liu, L. Xu, D.-X. Yan, H.-D. Huang, J.-H. Tang, J.-Z. Xu and Z.-M. Li, *Chem. Eng. J.*, 2019, **373**, 556–564.
7 J. S. Im, J. G. Kim and Y.-S. Lee, *Carbon*, 2009, **47**, 2640–2647.
8 Q. Chen, S. Yang, J. Bai and Y. Fu, *IEEE Trans. Antennas Propag.*, 2017, **65**, 4897–4902.
9 D.-X. Yan, H. Pang, B. Li, R. Vajtai, L. Xu, P.-G. Ren, J.-H. Wang and Z.-M. Li, *Adv. Funct. Mater.*, 2015, **25**, 559–566.
10 Z. Zeng, H. Jin, M. Chen, W. Li, L. Zhou and Z. Zhang, *Adv. Funct. Mater.*, 2016, **26**, 303–310.
11 M. Mahmoodi, M. Arjmand, U. Sundararaj and S. Park, *Carbon*, 2012, **50**, 1455–1464.
12 Y. Huang, N. Li, Y. Ma, F. Du, F. Li, X. He, X. Lin, H. Gao and Y. Chen, *Carbon*, 2007, **45**, 1614–1621.
13 J.-H. Lee, J. S. Oh, P. C. Lee, D. O. Kim, Y. Lee and J.-D. Nam, *J. Electron. Mater.*, 2008, **37**, 1648–1652.
14 R. Sun, H.-B. Zhang, J. Liu, X. Xie, R. Yang, Y. Li, S. Hong and Z.-Z. Yu, *Adv. Funct. Mater.*, 2017, **27**, 1702807.
15 J.-H. Lee, Y. Lee and J.-D. Nam, *Macromol. Rapid Commun.*, 2009, **30**, 52–56.
16 J.-H. Lee, D. O. Kim, G.-S. Song, Y. Lee, S.-B. Jung and J.-D. Nam, *Macromol. Rapid Commun.*, 2007, **28**, 634–640.
17 S. Kim, J.-B. Yoo, G.-R. Yi, Y. Lee, H. R. Choi, J. C. Koo, J.-S. Oh and J.-D. Nam, *J. Mater. Chem. C*, 2014, **2**, 6462–6466.
18 Y. Li, Y. Xu, T. Zhou, A. Zhang and J. Bao, *RSC Adv.*, 2015, **5**, 32469–32478.
19 W. L. Zhang, Y. D. Liu and H. J. Choi, *J. Mater. Chem.*, 2011, **21**, 6916–6921.
20 V. H. Pham, T. T. Dang, S. H. Hur, E. J. Kim and J. S. Chung, *ACS Appl. Mater. Interfaces*, 2012, **4**, 2630–2636.
21 Q. Shao, J. Tang, Y. Lin, F. Zhang, J. Yuan, H. Zhang, N. Shinya and L.-C. Qin, *J. Mater. Chem. A*, 2013, **1**, 15423–15428.
22 N. C. Das, Y. Liu, K. Yang, W. Peng, S. Maiti and H. Wang, *Polym. Eng. Sci.*, 2009, **49**, 1627–1634.
23 M. S. Kim, H. K. Kim, S. W. Byun, S. H. Jeong, Y. K. Hong, J. S. Joo, K. T. Song, J. K. Kim, C. J. Lee and J. Y. Lee, *Synth. Met.*, 2002, **126**, 233–239.
24 X. Shui and D. D. L. Chung, *J. Electron. Mater.*, 1997, **26**, 928–934.
25 M.-Y. Li, S. Gupta, C. Chang and N.-H. Tai, *Compos. B. Eng.*, 2019, **161**, 617–626.
26 M. H. Al-Saleh and U. Sundararaj, *Carbon*, 2009, **47**, 1738–1746.
27 M. H. Al-Saleh, W. H. Saadeh and U. Sundararaj, *Carbon*, 2013, **60**, 146–156.

28 H.-B. Zhang, Q. Yan, W.-G. Zheng, Z. He and Z.-Z. Yu, *ACS Appl. Mater. Interfaces*, 2011, **3**, 918–924.
29 M. Cao, X. Wang, W. Cao, X. Fang, B. Wen and J. Yuan, *Small*, 2018, **14**, 1800987.
30 X.-X. Wang, J.-C. Shu, W.-Q. Cao, M. Zhang, J. Yuan and M.-S. Cao, *Chem. Eng. J.*, 2019, **369**, 1068–1077.
31 M.-J. Hwang, M.-G. Kim, S. Kim, Y. C. Kim, H. W. Seo, J. K. Cho, I.-K. Park, J. Suhr, H. Moon, J. C. Koo, H. R. Choi, K. J. Kim, Y. Tak and J.-D. Nam, *Carbon*, 2019, **142**, 68–77.
32 Z. Tu, J. Wang, C. Yu, H. Xiao, T. Jiang, Y. Yang, D. Shi, Y.-W. Mai and R. K. Y. Li, *Compos. Sci. Technol.*, 2016, **134**, 49–56.
33 B. Wen, M. Cao, M. Lu, W. Cao, H. Shi, J. Liu, X. Wang, H. Jin, X. Fang, W. Wang and J. Yuan, *Adv. Mater.*, 2014, **26**, 3484–3489.
34 S. Taylor, Y. Yang and L. Wang, *J. Quant. Spectrosc. Radiat. Transfer*, 2017, **197**, 76–83.
35 F. Shahzad, M. Alhabeb, C. B. Hatter, B. Anasori, S. Man Hong, C. M. Koo and Y. Gogotsi, *Science*, 2016, **353**, 1137.
36 Q. Wei, S. Pei, X. Qian, H. Liu, Z. Liu, W. Zhang, T. Zhou, Z. Zhang, X. Zhang, H.-M. Cheng and W. Ren, *Adv. Mater.*, 2020, **32**, 1907411.
37 M. Han, X. Yin, H. Wu, Z. Hou, C. Song, X. Li, L. Zhang and L. Cheng, *ACS Appl. Mater. Interfaces*, 2016, **8**, 21011–21019.
38 U. Hwang, J. Kim, M. Seol, B. Lee, I.-K. Park, J. Suhr and J.-D. Nam, *ACS Omega*, 2022, **7**, 4135–4139.
39 R. Panwar, V. Agarwala and D. Singh, *Ceram. Int.*, 2015, **41**, 2923–2930.

